

1 **An iterative algorithm to simultaneously retrieve aerosol extinction and effective radius profiles using**
2 **the CALIOP lidar**

3 Liang Chang¹, Jing Li^{1,2#}, Jingjing Ren³, Changrui Xiong¹, Lu Zhang^{4,5}

4 ¹ *Department of Atmospheric and Oceanic Sciences, School of Physics, Peking University, Beijing 100871,*
5 *China*

6 ² *Collaborative Innovation Center on Forecast and Evaluation of Meteorological Disasters (CIC-FEMD),*
7 *Nanjing University of Information Science & Technology, Nanjing, 210044, China*

8 ³ *Intelligent Science & Technology Academy Limited of CASIC*

9 ⁴ *Key Laboratory of Radiometric Calibration and Validation for Environmental Satellites, National Satellite*
10 *Meteorological Center (National Center for Space Weather), China Meteorological Administration, Beijing*
11 *100081, China*

12 ⁵ *Innovation Center for FengYun Meteorological Satellite (FYSIC), Beijing 100081, China*

13 *# Correspondence to: Jing Li (jing-li@pku.edu.cn)*

14 **Abstract**

15 The Cloud-Aerosol Lidar with Orthogonal Polarization (CALIOP) onboard the Cloud-Aerosol Lidar and
16 Infrared Pathfinder Satellite Observation (CALIPSO) satellite has been widely used in climate and
17 environment studies to obtain the vertical profiles of atmospheric aerosols. To retrieve the vertical profile of
18 aerosol extinction, the CALIOP algorithm assumes column-averaged lidar ratios based on a clustering of
19 aerosol optical properties measured at surface stations. On one hand, these lidar ratio assumptions may not
20 be appropriate or representative at certain locations. On the other hand, the two-wavelength design of
21 CALIOP has the potential to constrain aerosol size information, which has not been considered in the
22 operational algorithm. In this study, we present a modified inversion algorithm to simultaneously retrieve
23 aerosol extinction and effective radius profiles using two-wavelength elastic lidars such as the CALIOP.

24 Specifically, a look-up table is built to relate the lidar ratio with the Ångström exponent calculated using
25 aerosol extinction at the two wavelengths, and the lidar ratio is then determined iteratively without a priori
26 assumption. The retrieved two-wavelength extinction at each layer is then converted to particle effective
27 radius assuming a lognormal distribution. The algorithm is tested on synthetic data, Raman lidar
28 measurements and then finally the real CALIOP backscatter measurements. Results show improvements over
29 the CALIPSO operational algorithm by comparing with ground-based Raman lidar profiles.

30 **1 Introduction**

31 Atmospheric aerosols have important impacts on the physical and chemical processes in atmosphere, as well
32 as the climate system and public health. Optical properties of aerosols are critical in quantifying their radiative
33 effects in the Earth's climate system. Moreover, the vertical distribution of aerosol properties, such as its
34 extinction coefficient and particle size, is one of the key elements to assess climate effect (IPCC, 2023).
35 Direct aerosol radiative forcing, which plays an important role in the Earth's energy budget, is impacted by
36 the vertical distribution of aerosols, especially that for absorbing aerosols (Goto et al., 2011; Eswaran et al.,
37 2019; Zhang et al., 2022). The vertical profiles of aerosol optical properties is also essential estimating the
38 solar heating rate (Kudo et al., 2016), and establishment of aerosol parameterization schemes for satellite
39 remote sensing (He et al., 2016). Although its importance is widely recognized, aerosol vertical distribution
40 is very difficult to monitor globally. Lidar is a major technique for obtaining the profiles of the aerosol
41 properties, which has been used in ground-based and satellite remote sensing systems. Especially, spaceborne
42 lidar is an effective way to observe the global distribution of aerosols. The Cloud-Aerosol Lidar with
43 Orthogonal Polarization (CALIOP) on the CALIPSO (The Cloud-Aerosol Lidar and Infrared Pathfinder
44 Satellite Observation) satellite, the only long-term orbiting spaceborne lidar to date, was launched on 28 April
45 2006. The CALIOP is a three-channel Mie-scattering lidar system, which contains two wavelengths of
46 532 *nm* (perpendicular & parallel polarization channel) and 1064 *nm*. It is the first polarization lidar to
47 provide three-channel elastic backscatter signals of global atmospheric measurements. The official aerosol

48 retrieval algorithm of CALIOP involves three modules, namely the Selective Iterated BoundarY Locator
49 (SIBYL), the Scene Classification Algorithm (SCA), and the Hybrid Extinction Retrieval Algorithms
50 (HERA). The HERA algorithm requires a lidar ratio (extinction-to-backscatter ratio of aerosols), which is
51 provided by the SCA. The SCA uses three CALIOP channels (532 *nm* parallel, 532 *nm* perpendicular and
52 1064 *nm* channels) to obtain the lidar ratio from the 6 groups of assumed column-averaged lidar ratios based
53 on a clustering of aerosol optical properties measured at surface stations (Winker et al., 2009).

54 The lidar ratio is dependent on the chemical composition, shape, particle size distribution of aerosols,
55 as well as the lidar wavelength (Burton et al., 2012), which is a critical parameter required for solving the
56 Mie-scattering lidar equation using the Klett (Klett, 1985) or Fernald (Fernald, 1984) methods. Previous
57 studies have developed algorithms to determine the lidar ratio iteratively for two-wavelength Mie scattering
58 lidars. Potter (1987) first introduced the two-wavelength lidar inversion technique to retrieve the aerosol
59 transmission with a constant lidar ratio in two independent wavelengths. Ackermann (Ackermann, 1997,
60 1998) developed an iterative method to obtain the variable lidar ratio from two-component (i.e., molecule
61 and aerosol) atmospheres by transcendental equation. Rajeev and Parameswaran (1998) proposed a new
62 method using the Mie theory calculated aerosol optical properties with Junge distribution of aerosols to
63 determine the lidar ratio by iteration. Lu et al. (2011) made an attempt to improve the two-wavelength lidar
64 inversion by iterative method, but failed to consider the size distribution of aerosols which may introduce
65 uncertainties in the inversion. Moreover, these studies mostly only gave the aerosol extinction profile without
66 retrieving the vertical distribution of aerosol size information. The algorithms were also mostly applied to
67 theoretical data or ground lidar measurements. The application to space lidars such as CALIOP is challenging
68 and thus limited.

69 In view of the above discussions, this study aims to provide a modified two-wavelength lidar
70 inversion algorithm to retrieve the vertical distribution of both aerosol extinction and particle effective radius,
71 avoiding the complex calculation confronted in the previous two-wavelength lidar inversion methods. The
72 algorithm is tested on synthetic data, surface Raman lidar and is finally applied to CALIOP measurements,

73 in order to better demonstrate its operational feasibility. The paper proceeds with descriptions of the inversion
 74 algorithm in Sect. 2. Sect. 3 presents the application of the algorithm to the Raman lidar and CALIOP with
 75 an analysis of retrieval uncertainties provided in Sect. 4. The study concludes in Sect. 5 with a brief discussion
 76 in the context of relevant lidar algorithms.

77 **2 Description of the lidar inversion algorithm**

78 The modified inversion algorithm retrieves the profiles of aerosol extinction and effective radius at two
 79 wavelengths, by solving the lidar equation using the Fernald method (Fernald, 1984) with a look-up table
 80 approach in the iteration procedure.

81 **2.1 Solving the lidar equation**

82 For each wavelength with a complete overlap between the fields of view of the laser and of the receiver, the
 83 lidar equation with calibration and range-correction can be expressed as:

$$84 \quad \beta'(R) = \frac{P(R)R^2}{E_0\xi} = [\beta_m(R) + \beta_p(R)]T_m^2(R)T_p^2(R), \quad (1)$$

85 where

$$86 \quad T^2(R) = e^{-2\tau(R)}, \quad (2)$$

$$87 \quad \tau(R) = \int_{R_0}^R \sigma(r)dr, \quad (3)$$

88 In Eq. (1-3), $\beta'(R)$ is the attenuated backscatter coefficients (calibrated and range-corrected signal)
 89 from distance R ; $P(R)$ is the measured signal after background subtraction and artefact removal from
 90 distance R ; E_0 is the average laser energy for the single-shot; ξ is the lidar system parameter; $\beta(R)$ and $\sigma(R)$
 91 are the volume backscatter and extinction coefficient at range R , respectively; $T^2(R)$ is the two-way
 92 transmittance from the lidar to the scattering volume at range R ; $\tau(R)$ is the optical depth at range R ; and the
 93 subscripts M and P denote the portions of air molecules and aerosols, respectively.

94 In order to facilitate calculation, the transmittance of air molecules $T_m^2(R)$ is separated from $\beta'(R)$
 95 to obtain the $E(R)$ as

$$96 \quad E(R) = \frac{\beta'(R)}{T_m^2(R)}, \quad (4)$$

97 As is well known, lidar back scatter signal is also subject to multiple scattering effects. These effects
 98 are typically small for low to moderate aerosol loading, and is only significant for optically thick clouds
 99 (Winker et al., 2009). Therefore, we neglect multiple scattering effects here and consider that the lidar ratio
 100 ($S(R)$) of aerosols is range dependent in single-scatter approximation, which can be written as

$$101 \quad S(R) = \frac{\sigma_p(R)}{\beta_p(R)}, \quad (5)$$

102 In the following, we use the Fernald method (Ackermann, 1998) to obtain the aerosol extinction
 103 coefficient at distance R as

$$104 \quad \sigma_p(R) = S(R) \left\{ E(R) e^{-2 \int_{R_0}^R S(r) \beta_m(r) dr} \left[C - 2 \int_{R_0}^R E(r) S(r) e^{-2 \int_{R_0}^r S(r') \beta_m(r') dr'} dr \right]^{-1} - \beta_m(R) \right\}, \quad (6)$$

105 where

$$106 \quad C = \frac{\beta'(R_0)}{\beta_p(R_0) + \beta_m(R_0)}, \quad (7)$$

107 The backscatter and extinction coefficient of air molecules can be determined with the Rayleigh
 108 scattering theory with the observed atmospheric profile (Bodhaine et al., 1999) as

$$109 \quad \sigma_m(R, \lambda) = \frac{C_s(\lambda) P(R)}{T(R)}, \quad (8)$$

$$110 \quad \beta_m(R, \lambda) = \frac{\sigma_m(R, \lambda)}{\frac{8\pi}{3} k_{b\omega}(\lambda)}, \quad (9)$$

111 Where $P(R)$ and $T(R)$ are the atmospheric pressure (hPa) and temperature (K) at distance R , respectively.
 112 $C_s(\lambda)$ and $k_{b\omega}(\lambda)$ are the atmospheric molecular constant related to the wavelength λ . Hostetler et al. (2006)
 113 suggested the values of $C_s(\lambda)$ and $k_{b\omega}(\lambda)$ at 532 nm and 1064 nm as $C_s(532 \text{ nm}) = 3.742 \times 10^{-6}$ (K/
 114 hPa/m); $C_s(1064 \text{ nm}) = 2.265 \times 10^{-7}$ (K/hPa/m); $k_{b\omega}(532 \text{ nm}) = 1.0313$; $k_{b\omega}(1604 \text{ nm}) = 1.0302$.

115 Thus, the aerosol extinction coefficient profiles can be obtained by Eq. (6) with an unknown variable
 116 of the lidar ratio. The two-wavelength lidar can give two independent profiles of attenuated backscatter

117 coefficients at different wavelengths, from which the aerosol extinction coefficient profiles can be calculated
 118 by assuming the lidar ratios at the two wavelengths.

119 For two wavelengths (λ_1 & λ_2), the Ångström exponent (AE) at distance R is defined as:

$$120 \quad AE(R) = -\frac{\ln\left[\frac{\sigma_p(R, \lambda_1)}{\sigma_p(R, \lambda_2)}\right]}{\ln\left[\frac{\lambda_1}{\lambda_2}\right]}, \quad (10)$$

121 Because AE is related to particle size distribution, which is a primary factor determining the lidar
 122 ratio, an AE -lidar ratio relationship can be established and used to determine the lidar ratio at each layer,
 123 which can then be used to retrieve aerosol extinction profiles from two-wavelength lidar measurements.

124 2.2 Look-up table

125 By assuming spherical particles size distribution, the aerosol extinction coefficients and backscatter
 126 coefficients can be calculated by Eq. (11-12):

$$127 \quad \sigma_p(\lambda) = \int_{r_{min}}^{r_{max}} Q_e(\lambda, r) \pi r^2 n(r) dr, \quad (11)$$

$$128 \quad \beta_p(\lambda) = \int_{r_{min}}^{r_{max}} Q_b(\lambda, r) \pi r^2 n(r) dr, \quad (12)$$

129 Where $n(r)$ represents the volume-size distribution of particles; r_{max} and r_{min} are the maximum and
 130 minimum of the particle radius, respectively; $Q_e(\lambda, r)$ and $Q_b(\lambda, r)$ denote the extinction and backscatter
 131 efficiencies of the particle (the scatter factor of the particle at 180°) with size r at wavelength λ , respectively.
 132 The size parameter is defined as $x \equiv 2\pi r / \lambda$, where $1 < x < 50$ for typical aerosols and thus the Mie
 133 scattering theory (Mishchenko and Yang, 2018) can be applied.

134 As the limited information provided by two-wavelength lidar, we assume the volume-size distribution
 135 of aerosols conform to the lognormal distribution, and the size distribution is expressed as follows (Deshler
 136 et al., 2003; Hara et al., 2021):

$$137 \quad n(r) = \frac{N}{r \ln s_d \sqrt{2\pi}} e^{-\frac{(\ln r - \ln r_0)^2}{2(\ln s_d)^2}}, \quad (13)$$

138 Where N is the total particle concentrations; r_0 and s_d are the median radius and the geometric standard
 139 deviation of aerosol size distribution, respectively. The particle size distribution is represented by its effective
 140 radius (\bar{r}) defined as:

$$141 \quad \bar{r} = \frac{\sum n(r)r^3}{\sum n(r)r^2}, \quad (14)$$

142 For convenient calculation, we assume a constant s_d for the each aerosol type, and the relationship between
 143 AE and \bar{r} can be established with given r_0 values.

144 We choose the six types of aerosols with their parameters in Table 1, which is consistent with the
 145 aerosol classification used in the operational algorithm of CALIOP (Winker et al., 2009). From Table 1, Type
 146 3 denotes the scattering aerosols, Type 2 shows both strong scattering and absorption, whereas other types
 147 are moderate scattering or absorbing. Combining Eqs. (5, 10-14), the relationship between Ångström
 148 exponent (AE) and lidar ratio (S), as well as that between AE and particle effective radius (\bar{r}) can be
 149 formulated as look-up tables for different refractive indices, as shown in Figure 1. Note that in Figure 1, it is
 150 easy to determine $S_{532 \text{ nm}}$, $S_{1064 \text{ nm}}$ and \bar{r} by the unique AE calculated from the lidar equation for a fixed
 151 aerosol type.

152 **2.3 The iterative inversion procedure**

153 After constructing the look-up table, we design the following iterative procedure to simultaneously retrieve
 154 aerosol extinction and effective radius profiles. Firstly, we calculate the extinction coefficients ($\sigma_{532 \text{ nm}}$ &
 155 $\sigma_{1064 \text{ nm}}$) of two wavelengths (532 nm & 1064 nm) from an initial guess of the lidar ratios ($S_{532 \text{ nm}}^0$ &
 156 $S_{1064 \text{ nm}}^0$) by solving the lidar equation (Eq. 6), then obtain the Ångström exponent (AE) through Eq. (10).
 157 Secondly, the look-up table are used to determine a set of new lidar ratios ($S'_{532 \text{ nm}}$ & $S'_{1064 \text{ nm}}$), which is
 158 used to calculate the new $\sigma_{532 \text{ nm}}$ & $\sigma_{1064 \text{ nm}}$ and Ångström exponent (AE'). This procedure is repeated until
 159 the difference between the updated AE' and previous AE reduces to a very small value (e.g., 10^{-3}). The final
 160 AE is converted to effective radius from the AE - \bar{r} look-up table, and the final values of $\sigma_{532 \text{ nm}}$, $\sigma_{1064 \text{ nm}}$,
 161 $S_{532 \text{ nm}}$, $S_{1064 \text{ nm}}$ and \bar{r} are the retrieved results of this layer. The above iterative algorithm is summarized
 162 into Figure 2.

163 Although in theory, our algorithm can retrieve aerosol extinction and effective radius at each layer,
 164 in reality the measurement noise may cause the inversion of certain layers fail to converge. In these cases,

165 we assume that this layer has the same aerosol type and size distribution as its adjacent layer, and then these
166 two layers are combined into a new layer to continue with the inversion.

167 **2.4 Test of the algorithm with synthetic data**

168 For verifying the feasibility of the inversion algorithm, we first conduct some retrieval tests using synthetic
169 data from Mie scattering and radiative transfer simulations. We assume a hypothesized profile of effective
170 radius, backscatter and extinction coefficients of the aerosols, and use the American atmospheric model in
171 1976 (National Geophysical Data, 1992) for molecular scattering, and calculate the attenuated backscatter
172 profiles according to the lidar equation. We then apply our algorithm to retrieve the aerosol property profiles
173 from these simulated lidar signals and compare them with the initial assumptions.

174 We only present the results for the reflective aerosol model, and results for other aerosol types are
175 similar. The simulated attenuated backscatter profiles for the two wavelengths are shown in Figure 3, and
176 the results of our inversion and their comparison with the assumed profiles are shown in Figure 4. It is clearly
177 seen that the results of the inversion are in good agreement with the assumed profiles. The MAPE (Mean
178 Absolute Percentage Error) between retrieved and assumed profiles of extinction coefficient, average particle
179 effective radius and lidar ratio are all below 0.1%, which proves the validity of the algorithm in theory. Note
180 that typically, selection of aerosol type is critical as incorrect assumption of aerosol refractive index will
181 result in divergence of the algorithm and thus yield no valid retrieval. This also helps us to determine the
182 appropriate aerosol type, i.e., the type that yields the best retrieval results.

183 **3 Application to real lidar measurements**

184 Before applying our algorithm to CALIOP measurements, we first use Raman lidar measurements to test its
185 accuracy as Raman lidars can directly retrieve aerosol extinction profiles without assuming a lidar ratio.

186 **3.1 Application to Raman lidar measurements**

187 A Raman lidar (Model LR231-D300, Raymetrics S.A, Greece) is installed on top of an 8-floor building at
188 the Peking University site (39°59'N, 116°18'E, 53m above sea level). It can provide the extinction and
189 backscatter coefficient at 532 nm by Raman inversion (Ansmann et al., 1990) without the need to assume
190 the lidar ratio. To test our inversion algorithm, we apply it to the elastic backscatter signals at 532 and 1064
191 nm and compare the retrieved extinction profile at 532 nm with that retrieved with the Raman method. Note
192 that the 1064 nm extinction is estimated using the Angstrom relationship of Eq. (10) and we assume that the
193 532 ~ 1064 nm AE equals the 355 ~ 532 nm AE. We apply the modified inversion algorithm to the cases
194 of four different aerosol types. To facilitate the determination of the initial value, we use the method of
195 remodelling downward attenuated backscatter from ground-based lidar (Tao et al., 2008) to reconstruct the
196 Raman lidar measurements at wavelength of 532 nm and 1064 nm, which are showing Figure 5-8(a).

197 We examined four cases in December 2017, as shown in Figures 5-8. The cases on 2 and 21 December
198 2017 both indicate that the extinction coefficient decreases sharply with altitude, and the maximum values
199 occur near the ground (Figure 6b & 7b). The other two cases on December 1 and 23 respectively show the
200 features of an elevated aerosol layer with maximum extinction found above the surface. In all four cases,
201 our retrieval results (red curves) agree well with those retrieved by the Raman method, with MAPE less than
202 30% in the extinction coefficient profiles. The lidar ratio profiles retrieved by our algorithm also agree well
203 with obtained from Raman method in some ranges, except these spikes at the highest or lowest point, may
204 be caused by the uncertainty of boundary. The aerosol particle effective radius slightly increases with altitude
205 and the peak (corresponding to $\sim 0.1 \mu\text{m}$) appear at ~ 0.7 km and ~ 1.7 km on 1 and 23 December 2017
206 (Figure 5d & 8d), respectively. Similar results were found by Zhang et al. (2009) and Cai et al. (2022) with
207 aircraft measurements over Beijing and the Loess Plateau in China respectively, which are mainly associated
208 with long range aerosol transport. The variability of particle effective radius profiles in Figure 6d is a typical
209 feature for low (and stable) PBL (Planetary Boundary Layer), which results in both particles and water vapor
210 accumulating near PBL top and thus remarkable hygroscopic growth of particle size may occur (Yang et al.,

211 2020). The case for Dec 21 (Figure 7d) shows relatively large particle size below~1.4km but sharply
212 decreases. This is likely related to the domination of local pollutions and insignificant PBL temperature
213 inversion (Li et al., 2022; Liu et al., 2009; Zhang et al., 2009).

214 **3.2 Application to CALIOP measurements**

215 We further apply our algorithm to real CALIOP measurements. To test its performance, we collocate
216 CALIOP profiles with those from surface-based Raman lidar measurement within the European Aerosol
217 Research Lidar NETwork (EARLINET, www.earlinet.org, (Matthias et al., 2004). Aerosol profiles from the
218 Napoli (southern Italy, 40.838 °N , 14.183 °E , 118 m above sea level), Evora (south-central
219 Portugal, 38.5678 °N, -7.9115 °E, 293 m above sea level) and Warsaw (east-central, 52.21 °N, 20.98 °E,
220 112m above sea level) stations have the best match with CALIOP and high data quality in cloudless sky, are
221 primarily used to validate the retrieval results. The CALIPSO overpass times for the chosen cases and the
222 corresponding horizontal distances between the sub-satellite point and ground-based Raman lidar site are
223 listed in Table 2.

224 To compare with the lidar returns measured by CALIOP (down-looking) and ground-based Raman
225 lidar (up-looking), we still use the method of remodelling downward attenuated backscatter from ground-
226 based lidar (Tao et al., 2008) to reconstruct the downward attenuated backscatter signals for the ground-based
227 Raman lidar. The attenuated backscatter signals of CALIOP was averaged for 163 nearby sub-satellite point
228 profiles (CALIPSO ground track range of about 30 km within 8 s) (Lu et al., 2011; Wang et al., 2007),
229 obtained from CALIOP level 1B products, to improve the signal-to-noise ratio.

230 The attenuated backscatter profiles at 532 nm from CALIOP agree well with those from the Napoli
231 Raman Lidar (NRL), as shown in Figures 9-14(a). The initial altitude of inversion (the upper boundary of the
232 aerosol layer) is determined by the variation of attenuated backscatter signal and volume linear depolarization
233 ratio at 532 nm. Comparison between our inversion results, CALIOP operational results and Raman results
234 is shown in Figure 9-14(c).

235 The CALIOP operational product only provides retrievals for three cases considered, namely 20
236 August 2006, 20 June 2007 and 22 July 2007. In all three cases, the aerosol extinction profiles of our
237 algorithm (red curve) appear in better consistency with Raman lidar results, and our algorithm reduces the
238 mean MAPE between the retrieval of extinction profiles in CALIOP and Raman lidar from 74% (CALIOP
239 operational product) to 37%. Our algorithm successfully corrects the overestimation for the August 20, 2006
240 and July 22, 2007 cases. For the June 20, 2007 case, the operational results show a lower peak at ~1.7 km
241 and a secondary peak at ~4 km, both of which are absent in the Raman profile, and our results agree well
242 with Raman in both the shape and magnitude. In the other three cases, CALIOP does not provide Level 2
243 retrieval results. Our algorithm is able to retrieve and the extinction profiles agree well with Raman lidar
244 observations. Our retrievals do show more fluctuations compared to Raman lidar, possibly due to the noises
245 in the attenuated backscatter profiles of CALIOP. Because Raman lidar does not provide retrieval of aerosol
246 effective radius profiles, we compare the lidar ratio profiles by our algorithm and the Raman algorithm.
247 Overall, our algorithm produces lidar ratios varying in a relatively small range around 50, whereas Raman
248 lidar ratios can vary from ~10 to 200. Also, the Raman lidar ratios tend to change sharply at the highest or
249 lowest point, which may be caused by the inversion errors at the boundary. By removing these spikes, the
250 differences of the lidar ratio between CALIOP and Raman is obviously reduced. In general, the aerosol
251 particle effective radius increases with altitude, similar to Figures 5d and 8d, but the fluctuations of the
252 profiles may also be caused the noise in the CALIOP measurement.

253 When examining the CALIOP backscatter measurements, we found that the backscatter signal at 1064
254 nm is often stronger than that at 532 nm after 2010, which is unphysical and possibly due to issues such as
255 calibration and lidar degradation. As a result, the remodeled backscatter profiles of CALIOP appear noisier
256 and do not exactly match those from Raman lidar for the Evora and Warsaw stations, which only have
257 collocated measurements in 2019 and 2020 (Figure 15-19a). Our retrieved extinction profiles also agree
258 reasonably well with those by Raman lidar (Figure 15-19b), with the lidar ratio profiles and aerosol particle
259 effective radius profiles similar to the cases at Naples. By contrast, the extinction profiles of the official

260 CALIPSO product show large deviations from the Raman profile with unphysical spikes (Figure 16b),
261 incomplete profiles (Figure 17&18b) or no retrievals (Figure 15b).

262 **4 Uncertainty analysis**

263 Uncertainties in aerosol extinction and effective radius profiles retrieved by our two-wavelength inversion
264 algorithm are mainly due to measurement noise (e.g., the signal statistical error, the estimations of molecular
265 optical properties, etc.), calibration errors, and assumption errors. In this section, we further examine the
266 errors associated with the assumptions in the algorithm.

267 First, the single-scattering approximation is used in solving lidar equation, as multiple scattering effects
268 in aerosol layers are generally small and are currently neglected for CALIOP (Winker et al., 2009). We limit
269 the application of our algorithm to clear sky weather conditions to reduce this error, but this error is very
270 difficult to quantify.

271 Second, the errors in the aerosol refractive index, size distribution and sphericity assumptions in look-up
272 tables can also introduce errors in solving the lidar equation. The lognormal distribution assumption of
273 aerosol volume-size distribution may make the algorithm fail to converge in other actual size distributions.
274 For example, using data generated by Junge distribution (a simpler aerosol size distribution), the algorithm
275 cannot yield valid retrieval results. Similar outcome is noted for non-spherical particles or aerosol types
276 significantly different from the assumed type.

277 Finally, we consider assumption and retrieval uncertainties as a perturbation in the lidar ratio and attempt
278 to quantify its effect on the retrieved profiles. We increase the lidar ratio profiles at 532 nm and 1064 nm
279 from the look-up tables by $\pm 10\%$ before calculating the synthetic attenuated backscatter profiles, which
280 makes the synthetic data do not entirely match the look-up table. The retrieval profiles exhibit mean MAPE
281 less than 14% (in 10% case) and 17% (in -10% case), indicating that the algorithm is comparatively robust
282 to noise.

283 **5 Summary and discussion**

284 In this study, we described a modified lidar inversion algorithm to retrieve aerosol extinction and size
285 distribution simultaneously from two wavelengths elastic lidar measurements. Its major advantage over the
286 operational CALIOP algorithm is that the lidar ratio of each layer is determined iteratively by the lidar ratio-
287 AE look-up table. The algorithm was applied to the ground-based Raman lidar measurements at the PKU
288 site, as well as to CALIOP measurements. The comparison results indicate that the retrieved aerosol
289 extinction coefficient profiles by our method using CALIOP attenuated backscatter measurements are in
290 good agreement with Raman lidar measurements. Characteristics of aerosol effective radius profiles are also
291 retrieved, which can be used as a reference for aerosols size information.

292 In comparison with the iterative method by transcendental equation (Ackermann, 1997, 1998), our
293 inversion uses the look-up table to simplify the complex calculation. Cao et al. (2019) develop a lidar-ratio
294 iteration method to invert the particle-size distribution with assumed Junge distribution, but the method was
295 just used in simple simulation without actual tests. Although Lu et al. (2011) invert the aerosol backscatter
296 coefficient profiles from CALIPSO lidar measurements by iterative method, failed to consider the size
297 distribution of aerosols which may introduce uncertainties in the inversion. Compared with other modified
298 CALIOP inversions by combining other measurements, such as ground-based lidar (Wang et al., 2007), our
299 inversion is weaker by the space-time limitations.

300 However, this study still bears certain limitations. The current algorithm is primarily suitable for fine
301 mode spherical particles, such as urban pollution, and considers the change of aerosol size (thus lidar ratio)
302 with altitude, due to long range transport, vertical mixing, hygroscopic growth, etc. Non-spherical particles
303 such as dust will be explored in the next step, possibly by taking advantage of the depolarization ratio
304 (Gialitaki et al., 2020; Kahnert et al., 2020; Luo et al., 2022; Luo et al., 2019) measurement that is not used
305 here. Another drawback is that although the algorithm does not need to assume a lidar ratio, the complex
306 refractive index still needs to be assumed. As discussed above, the lidar ratio is very sensitive to the imaginary
307 part and an incorrect assumption may induce errors or even makes the algorithm unable to converge.

308 Therefore, this algorithm is mostly suitable when there is no significant change in aerosol type vertically.
309 Finally, the polarization channel of CALIOP may contain additional aerosol type information but is only
310 used when determining the initial refractive index (excluding dust) here. We also plan to refine our look-up
311 table by incorporating polarization in order to improve the accuracy of the retrieval.

312 **Data availability**

313 All raw data can be provided by the corresponding authors upon request.

314 **Author contributions**

315 LC and JL planned the research; LC, JL, JR, CX, and LZ developed the algorithm; LC and JL analyzed the
316 results; LC and JL wrote the manuscript.

317 **Competing interests**

318 The authors declare that they have no conflict of interest.

319 **Acknowledgement**

320 This study is funded by the National Key Research and Development Program of China (grant no.
321 2023YFF0805401) and National Natural Science Foundation of China (NSFC) Grant No. 42175144.

322 **References**

- 323 Ackermann, J.: Two-wavelength lidar inversion algorithm for a two-component atmosphere, *Appl. Opt.*, 36,
324 5134-5143, 10.1364/AO.36.005134, 1997.
- 325 Ackermann, J.: Two-wavelength lidar inversion algorithm for a two-component atmosphere with variable
326 extinction-to-backscatter ratios, *Appl. Opt.*, 37, 3164-3171, 10.1364/AO.37.003164, 1998.
- 327 Ansmann, A., Riebesell, M., and Weitkamp, C.: Measurement of atmospheric aerosol extinction profiles with
328 a Raman lidar, *Opt. Lett.*, 15, 746-748, 10.1364/OL.15.000746, 1990.
- 329 Bodhaine, B. A., Wood, N. B., Dutton, E. G., and Slusser, J. R.: On Rayleigh Optical Depth Calculations,
330 *Journal of Atmospheric and Oceanic Technology*, 16, 1854-1861, 10.1175/1520-
331 0426(1999)016<1854:orodc>2.0.co;2, 1999.
- 332 Burton, S. P., Ferrare, R. A., Hostetler, C. A., Hair, J. W., Rogers, R. R., Obland, M. D., Butler, C. F., Cook,
333 A. L., Harper, D. B., and Froyd, K. D.: Aerosol classification using airborne High Spectral Resolution
334 Lidar measurements – methodology and examples, *Atmos. Meas. Tech.*, 5, 73-98, 10.5194/amt-5-73-
335 2012, 2012.
- 336 Cai, Z., Li, Z., Li, P., Li, J., Sun, H., Yang, Y., Gao, X., Ren, G., Ren, R., and Wei, J.: Vertical distributions
337 of aerosol microphysical and optical properties based on aircraft measurements made over the Loess
338 Plateau in China, *Atmospheric Environment*, 270, 118888,
339 <https://doi.org/10.1016/j.atmosenv.2021.118888>, 2022.
- 340 Cao, N., Yang, S., Cao, S., Yang, S., and Shen, J.: Accuracy calculation for lidar ratio and aerosol size
341 distribution by dual-wavelength lidar, *Applied Physics A*, 125, 590, 10.1007/s00339-019-2819-y,
342 2019.
- 343 Deshler, T., Hervig, M. E., Hofmann, D. J., Rosen, J. M., and Liley, J. B.: Thirty years of in situ stratospheric
344 aerosol size distribution measurements from Laramie, Wyoming (41°N), using balloon-borne
345 instruments, *Journal of Geophysical Research: Atmospheres*, 108, 10.1029/2002jd002514, 2003.

346 Eswaran, K., Satheesh, S. K., and Srinivasan, J.: Sensitivity of aerosol radiative forcing to various aerosol
347 parameters over the Bay of Bengal, *Journal of Earth System Science*, 128, 170, 10.1007/s12040-019-
348 1200-z, 2019.

349 Fernald, F. G.: Analysis of atmospheric lidar observations: some comments, *Appl. Opt.*, 23, 652-653,
350 10.1364/AO.23.000652, 1984.

351 Gialitaki, A., Tsekeri, A., Amiridis, V., Ceolato, R., Paulien, L., Kampouri, A., Gkikas, A., Solomos, S.,
352 Marinou, E., Haarig, M., Baars, H., Ansmann, A., Lapyonok, T., Lopatin, A., Dubovik, O., Groß, S.,
353 Wirth, M., Tschla, M., Tsikoudi, I., and Balis, D.: Is the near-spherical shape the “new black” for
354 smoke?, *Atmos. Chem. Phys.*, 20, 14005-14021, 10.5194/acp-20-14005-2020, 2020.

355 Goto, D., Nakajima, T., Takemura, T., and Sudo, K.: A study of uncertainties in the sulfate distribution and
356 its radiative forcing associated with sulfur chemistry in a global aerosol model, *Atmos. Chem. Phys.*,
357 11, 10889-10910, 10.5194/acp-11-10889-2011, 2011.

358 Hara, K., Nishita-Hara, C., Osada, K., Yabuki, M., and Yamanouchi, T.: Characterization of aerosol number
359 size distributions and their effect on cloud properties at Syowa Station, Antarctica, *Atmos. Chem.*
360 *Phys.*, 21, 12155-12172, 10.5194/acp-21-12155-2021, 2021.

361 He, Q., Li, C., Geng, F., Zhou, G., Gao, W., Yu, W., Li, Z., and Du, M.: A parameterization scheme of aerosol
362 vertical distribution for surface-level visibility retrieval from satellite remote sensing, *Remote*
363 *Sensing of Environment*, 181, 1-13, <https://doi.org/10.1016/j.rse.2016.03.016>, 2016.

364 Hostetler, C., Liu, Z., Reagan, J., Vaughan, M., Winker, D., Osborn, M., Hunt, W., Powell, K., and Trepte,
365 C.: CALIOP algorithm theoretical basis document calibration and Level 1 data products, Hampton,
366 VA: NASA Langley Research Center, 2006.

367 IPCC: Climate Change 2021 – The Physical Science Basis: Working Group I Contribution to the Sixth
368 Assessment Report of the Intergovernmental Panel on Climate Change, Cambridge University Press,
369 Cambridge, DOI: 10.1017/9781009157896, 2023.

370 Josset, D., Rogers, R., Pelon, J., Hu, Y., Liu, Z., Omar, A., and Zhai, P.-W.: CALIPSO lidar ratio retrieval
371 over the ocean, *Opt. Express*, 19, 18696-18706, 10.1364/OE.19.018696, 2011.

372 Kahnert, M., Kanngießer, F., Järvinen, E., and Schnaiter, M.: Aerosol-optics model for the backscatter
373 depolarisation ratio of mineral dust particles, *Journal of Quantitative Spectroscopy and Radiative*
374 *Transfer*, 254, 107177, <https://doi.org/10.1016/j.jqsrt.2020.107177>, 2020.

375 Klett, J. D.: Lidar inversion with variable backscatter/extinction ratios, *Appl. Opt.*, 24, 1638-1643,
376 10.1364/AO.24.001638, 1985.

377 Kudo, R., Nishizawa, T., and Aoyagi, T.: Vertical profiles of aerosol optical properties and the solar heating
378 rate estimated by combining sky radiometer and lidar measurements, *Atmos. Meas. Tech.*, 9, 3223-
379 3243, 10.5194/amt-9-3223-2016, 2016.

380 Li, Y., Guo, X., Jin, L., Li, P., Sun, H., Zhao, D., and Ma, X.: Aircraft Measurements of Summer Vertical
381 Distributions of Aerosols and Transitions to Cloud Condensation Nuclei and Cloud Droplets in
382 Central Northern China, *Chinese Journal of Atmospheric Sciences*, 46, 845, 10.3878/j.issn.1006-
383 9895.2104.20255, 2022.

384 Liu, P., Zhao, C., Zhang, Q., Deng, Z., Huang, M., Ma, X., and Tie, X.: Aircraft study of aerosol vertical
385 distributions over Beijing and their optical properties, *Tellus B*, 61, 756-767,
386 <https://doi.org/10.1111/j.1600-0889.2009.00440.x>, 2009.

387 Lu, X., Jiang, Y., Zhang, X., Wang, X., and Spinelli, N.: Two-wavelength lidar inversion algorithm for
388 determination of aerosol extinction-to-backscatter ratio and its application to CALIPSO lidar
389 measurements, *Journal of Quantitative Spectroscopy and Radiative Transfer*, 112, 320-328,
390 <https://doi.org/10.1016/j.jqsrt.2010.07.013>, 2011.

391 Luo, J., Zhang, Q., Luo, J., Liu, J., Huo, Y., and Zhang, Y.: Optical Modeling of Black Carbon With Different
392 Coating Materials: The Effect of Coating Configurations, *Journal of Geophysical Research:*
393 *Atmospheres*, 124, 13230-13253, <https://doi.org/10.1029/2019JD031701>, 2019.

394 Luo, J., Li, Z., Fan, C., Xu, H., Zhang, Y., Hou, W., Qie, L., Gu, H., Zhu, M., Li, Y., and Li, K.: The
395 polarimetric characteristics of dust with irregular shapes: evaluation of the spheroid model for single
396 particles, *Atmos. Meas. Tech.*, 15, 2767-2789, 10.5194/amt-15-2767-2022, 2022.

397 Matthias, V., Freudenthaler, V., Amodeo, A., Balin, I., Balis, D., Bosenberg, J., Chaikovsky, A., Chourdakis,
398 G., Comeron, A., Delaval, A., De Tomasi, F., Eixmann, R., Hagard, A., Komguem, L., Kreipl, S.,
399 Matthey, R., Rizi, V., Rodrigues, J., Wandinger, U., and Wang, X.: Aerosol lidar intercomparison in
400 the framework of the EARLINET project. 1. Instruments (vol 43, pg 976, 2004), *Appl. Opt.*, 43, 2004.

401 Mishchenko, M. I. and Yang, P.: Far-field Lorenz–Mie scattering in an absorbing host medium: Theoretical
402 formalism and FORTRAN program, *Journal of Quantitative Spectroscopy and Radiative Transfer*,
403 205, 241-252, <https://doi.org/10.1016/j.jqsrt.2017.10.014>, 2018.

404 National Geophysical Data, C.: U.S. standard atmosphere (1976), *Planetary and Space Science*, 40, 553-554,
405 [https://doi.org/10.1016/0032-0633\(92\)90203-Z](https://doi.org/10.1016/0032-0633(92)90203-Z), 1992.

406 Potter, J. F.: Two-frequency lidar inversion technique, *Appl. Opt.*, 26, 1250-1256, 10.1364/AO.26.001250,
407 1987.

408 Rajeev, K. and Parameswaran, K.: Iterative method for the inversion of multiwavelength lidar signals to
409 determine aerosol size distribution, *Appl. Opt.*, 37, 4690-4700, 10.1364/AO.37.004690, 1998.

410 Tao, Z., McCormick, M. P., and Wu, D.: A comparison method for spaceborne and ground-based lidar and
411 its application to the CALIPSO lidar, *Applied Physics B*, 91, 639, 10.1007/s00340-008-3043-1, 2008.

412 Wang, X., Frontoso, M. G., Pisani, G., and Spinelli, N.: Retrieval of atmospheric particles optical properties
413 by combining ground-based and spaceborne lidar elastic scattering profiles, *Opt. Express*, 15, 6734-
414 6743, 10.1364/OE.15.006734, 2007.

415 Winker, D. M., Vaughan, M. A., Omar, A., Hu, Y., Powell, K. A., Liu, Z., Hunt, W. H., and Young, S. A.:
416 Overview of the CALIPSO Mission and CALIOP Data Processing Algorithms, *Journal of*
417 *Atmospheric and Oceanic Technology*, 26, 2310-2323, 10.1175/2009jtecha1281.1, 2009.

418 Yang, J., Li, J., Li, P., Sun, G., Cai, Z., Yang, X., Cui, C., Dong, X., Xi, B., Wan, R., Wang, B., and Zhou,
419 Z.: Spatial Distribution and Impacts of Aerosols on Clouds Under Meiyu Frontal Weather
420 Background Over Central China Based on Aircraft Observations, *Journal of Geophysical Research:*
421 *Atmospheres*, 125, e2019JD031915, <https://doi.org/10.1029/2019JD031915>, 2020.

422 Zhang, L., Li, J., Jiang, Z., Dong, Y., Ying, T., and Zhang, Z.: Clear-Sky Direct Aerosol Radiative Forcing
423 Uncertainty Associated with Aerosol Optical Properties Based on CMIP6 Models, *Journal of Climate*,
424 35, 3007-3019, <https://doi.org/10.1175/JCLI-D-21-0479.1>, 2022.

425 Zhang, Q., Ma, X., Tie, X., Huang, M., and Zhao, C.: Vertical distributions of aerosols under different
426 weather conditions: Analysis of in-situ aircraft measurements in Beijing, China, *Atmospheric*
427 *Environment*, 43, 5526-5535, <https://doi.org/10.1016/j.atmosenv.2009.05.037>, 2009.

428

429

430 **Table 1.** The aerosols parameters of the look-up table. m_r denotes the real part of the refractive index, m_i
 431 denotes the imaginary part of the refractive index, and s_d is the standard deviation of the lognormal size
 432 distribution.

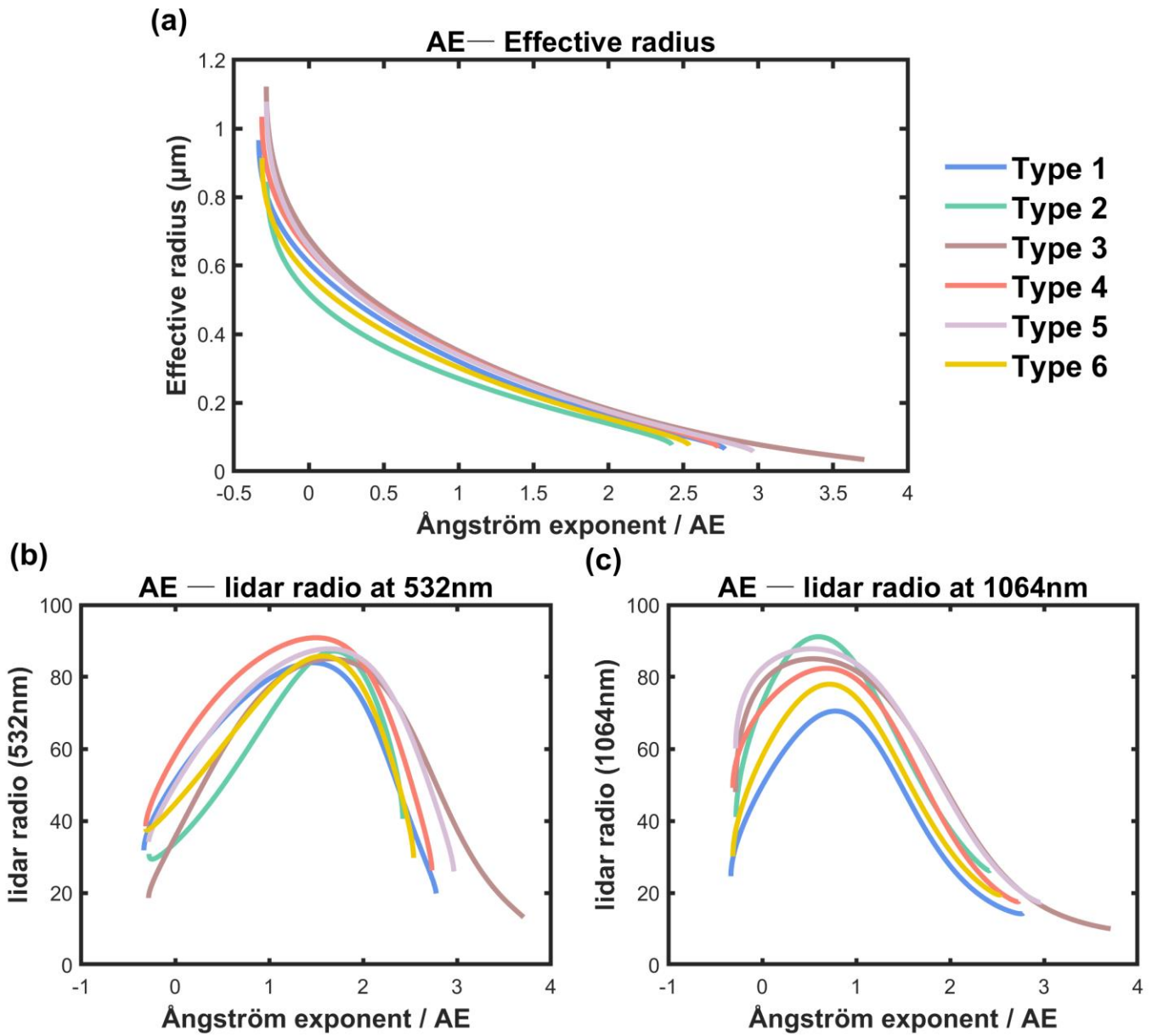
	Type 1	Type 2	Type 3	Type 4	Type 5	Type 6
m_r (532 nm)	1.414	1.517	1.380	1.404	1.400	1.452
m_i (532 nm)	0.0036	0.0234	0.0001	0.0063	0.0050	0.0109
m_r (1064 nm)	1.495	1.541	1.380	1.439	1.400	1.512
m_i (1064 nm)	0.0043	0.0298	0.0001	0.0073	0.0050	0.0137
s_d	1.4813	1.5624	1.6100	1.5257	1.6000	1.5112

433

434 **Table 2.** Information of collocated EARLINET and CALIPSO cases.

435

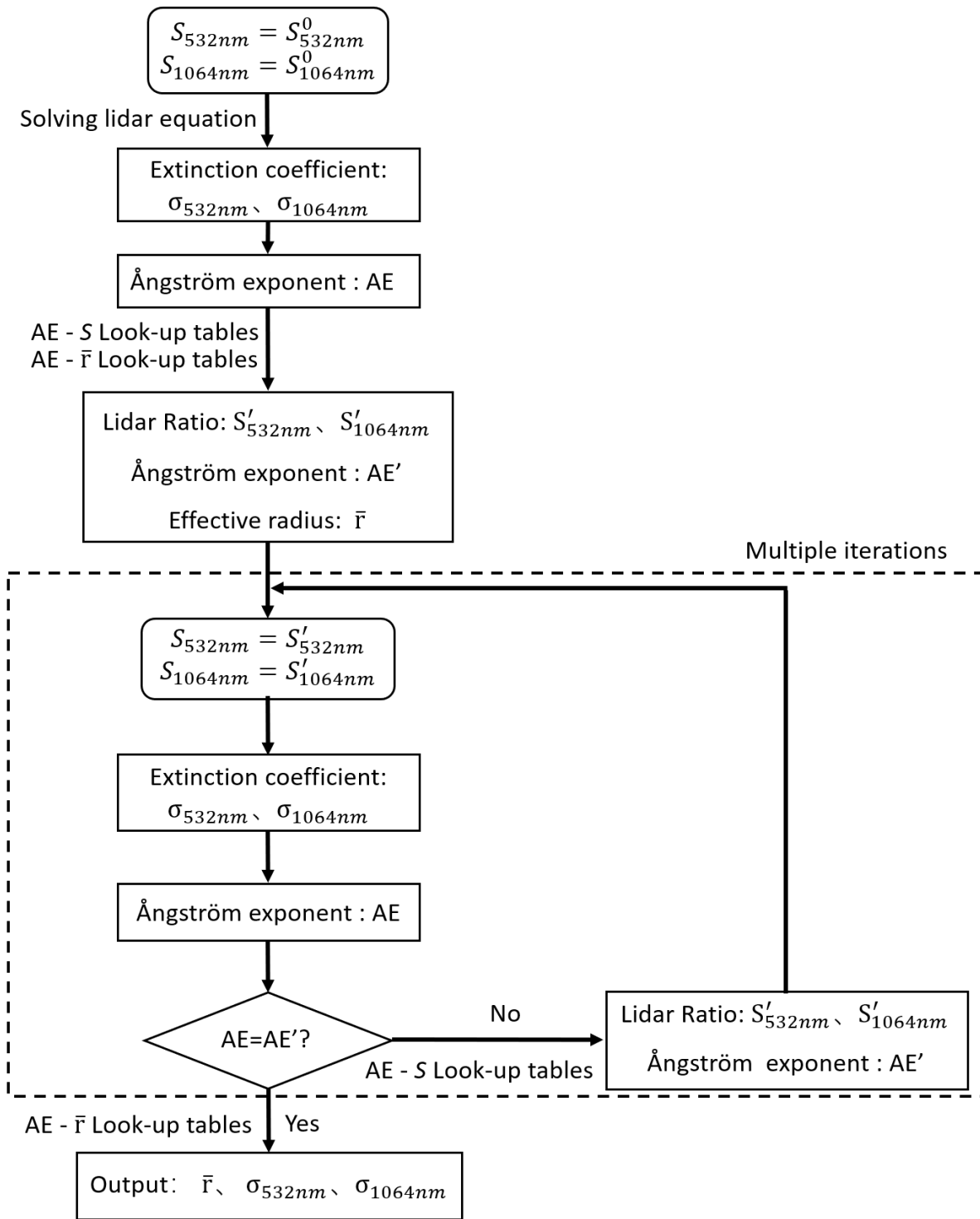
Station	Time (UTC)	Horizontal distance (km)
	2006-08-20 01:17:25	0.0708
	2007-06-20 01:17:57	0.0808
	2008-07-08 01:18:43	0.0690
Napoli	2008-08-02 01:13:02	1.3246
	2008-08-09 01:19:14	0.0807
	2009-09-29 01:21:03	0.0778
	2019-04-05 02:47:48	0.0863
Evora	2020-01-13 02:54:00	0.0164
	2020-03-18 02:55:43	0.0009
	2015-08-15 01:19:14	< 0.0001
Warsaw	2020-03-31 01:13:38	0.0177



436

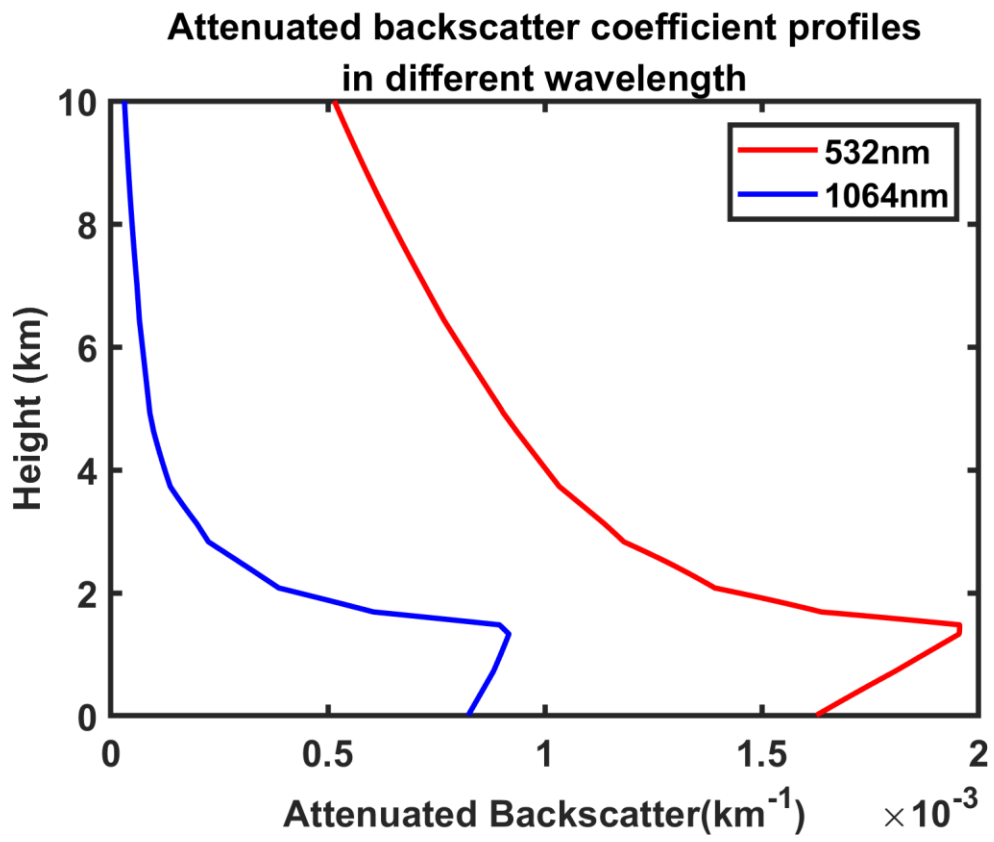
437 **Figure 1.** The Look-up tables for (a) AE-effective radius, (b) AE-lidar ratio at 532 nm and (c) AE-

438 lidar ratio at 1064 nm. The AE is calculated using 532 nm and 1064 nm aerosol extinction coefficients.



439

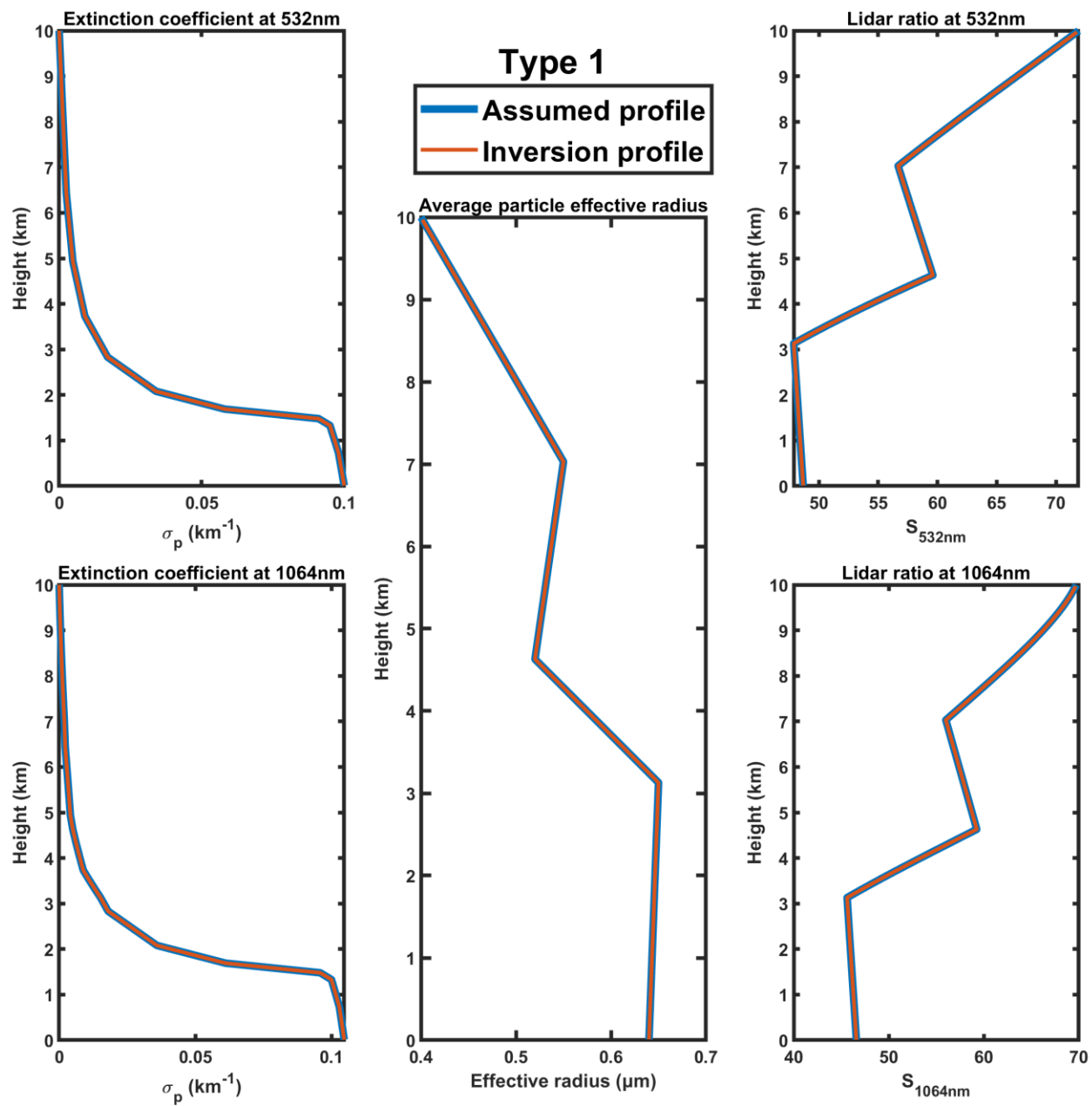
440 **Figure 2.** Schematic of the inversion algorithm (λ_1 and λ_2 represent the two different wavelengths,
 441 respectively; S is the lidar ratio; σ is the aerosol extinction; AE is the Ångström index; \bar{r} is the average
 442 particle effective radius; S^0 is the initial value of lidar ratio; S' and AE' are the look up values of lidar ratio
 443 and Ångström index, respectively.)



444

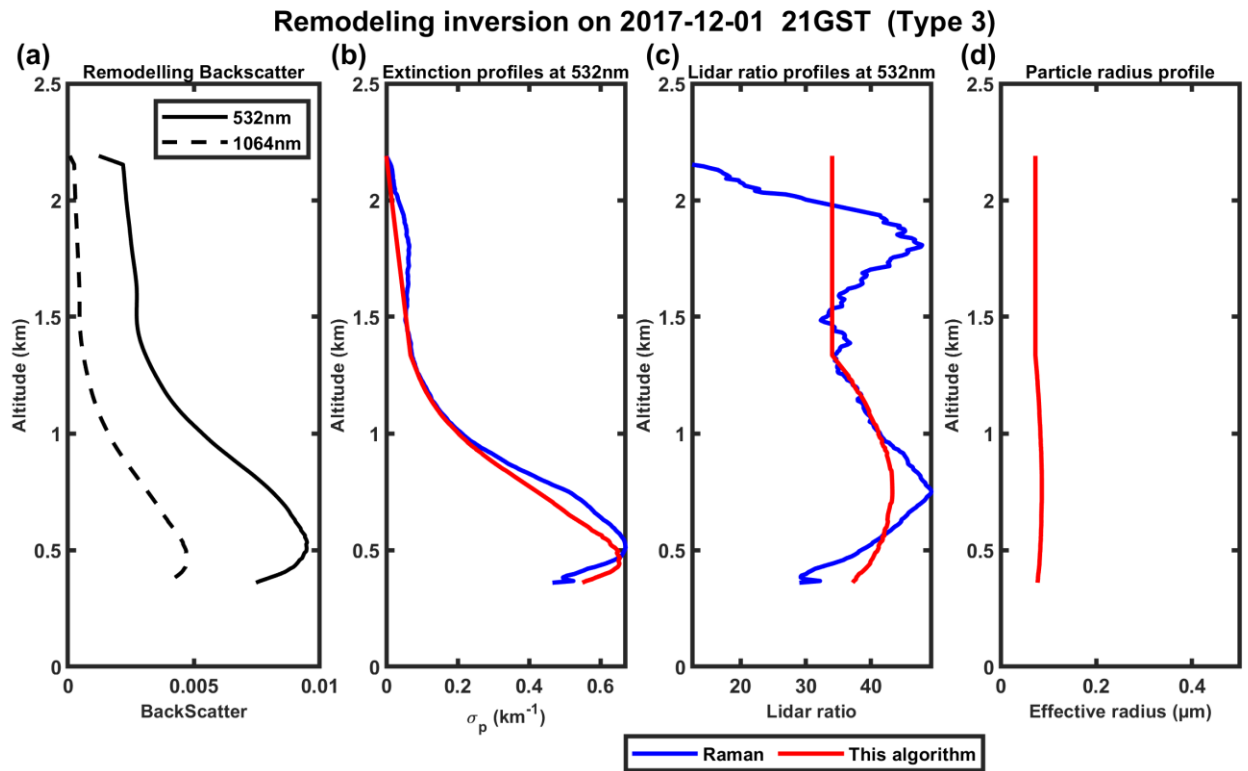
445

Figure 3. The attenuated backscatter coefficient profiles at different wavelengths using synthetic data.



446

447 **Figure 4.** The result of the inversion algorithm using the synthetic data shown in Figure 3.

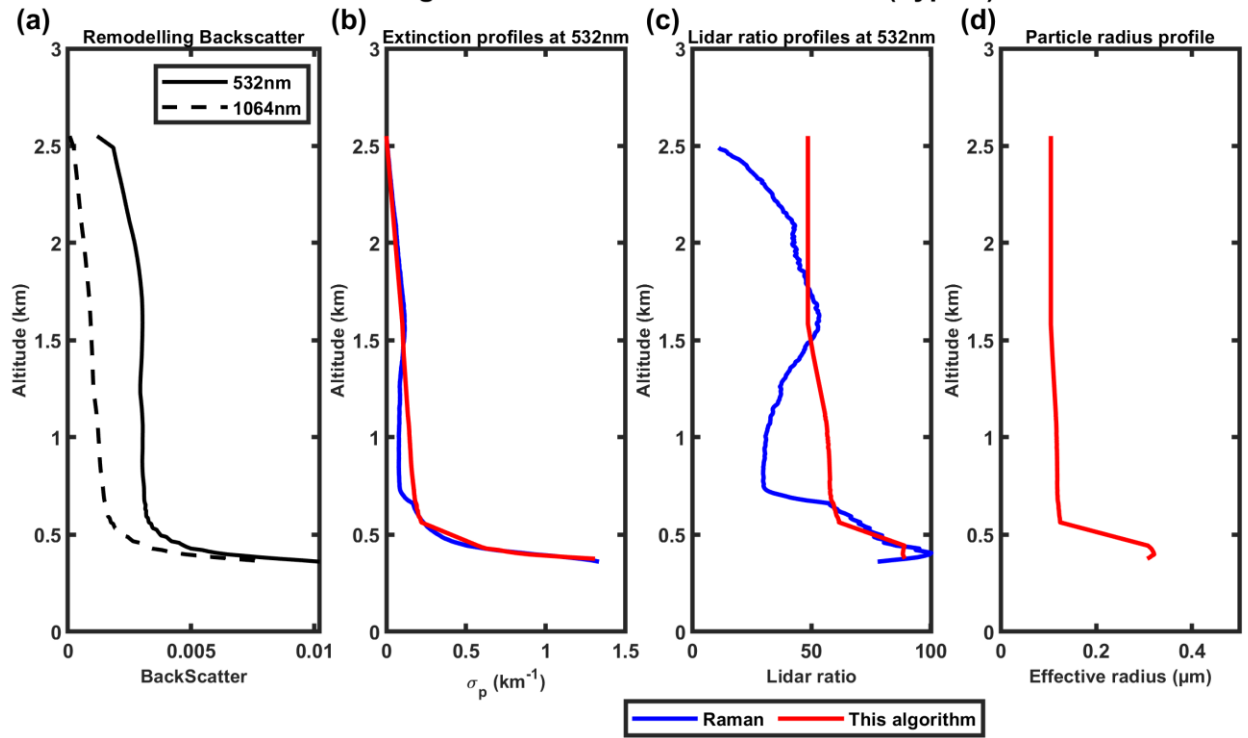


448

449 **Figure 5.** (a) Remodeled downward attenuated backscatter profiles measured by Raman lidar in PKU on 1
 450 December 2017; (b) show the extinction profiles inverted by the modified inversion algorithm (red) and
 451 Raman (blue); (c) shows the particle effective radius profiles.

452

Remodeling inversion on 2017-12-02 21GST (Type 4)



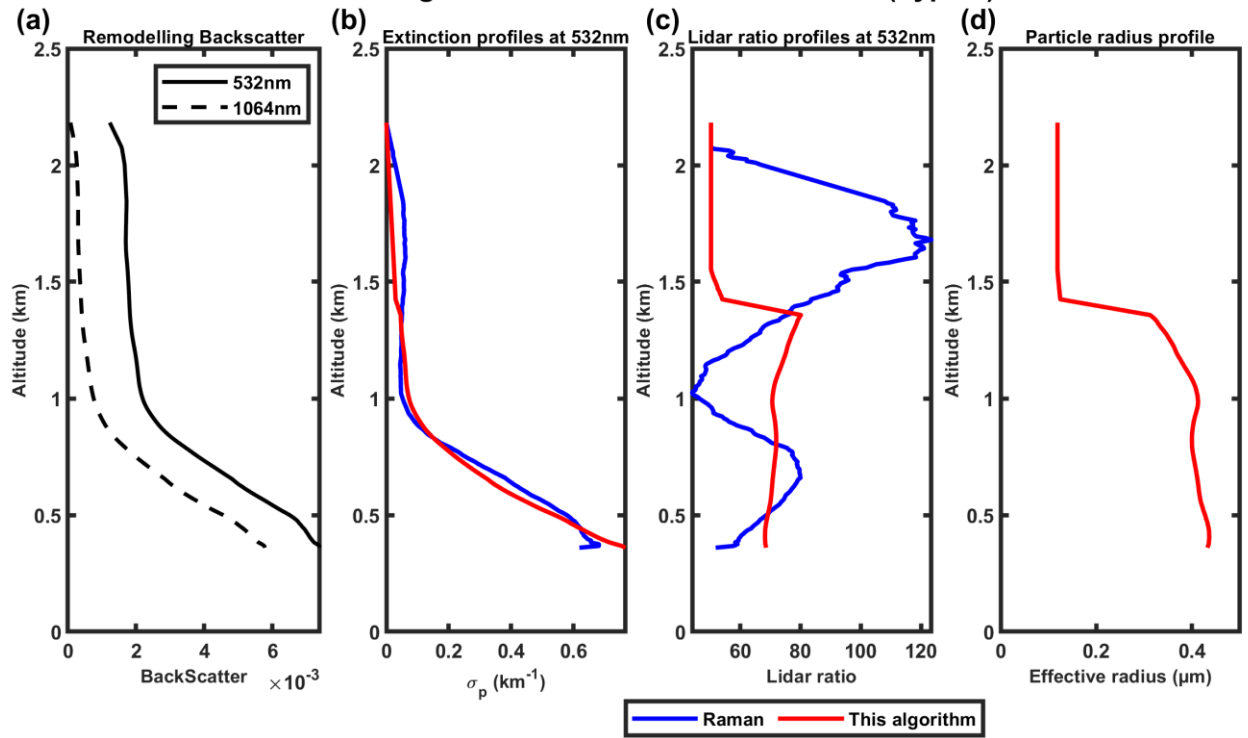
453

454

455

Figure 6. Same as Figure 5 but on 2 December 2017.

Remodeling inversion on 2017-12-21 20GST (Type 1)



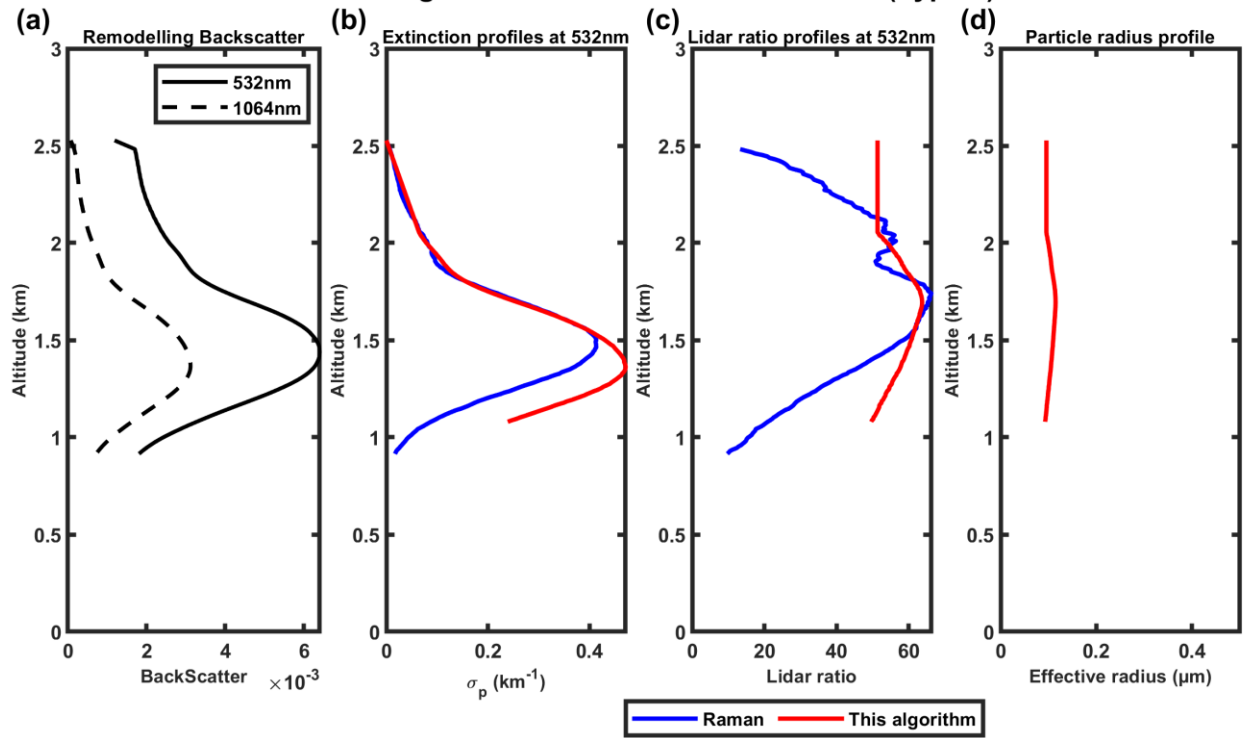
456

457

458

Figure 7. Same as Figure 5 but on 21 December 2017.

Remodeling inversion on 2017-12-23 02GST (Type 5)



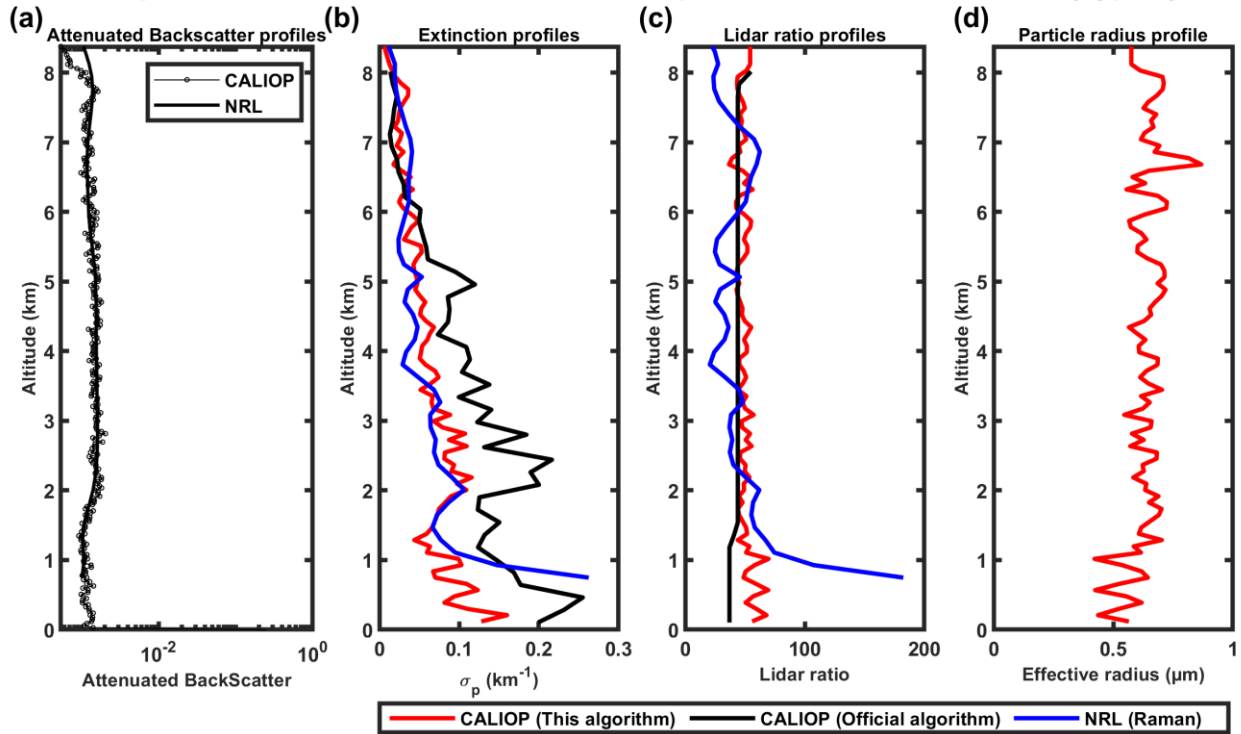
459

460

461

Figure 8. Same as Figure 5 but on 23 December 2017.

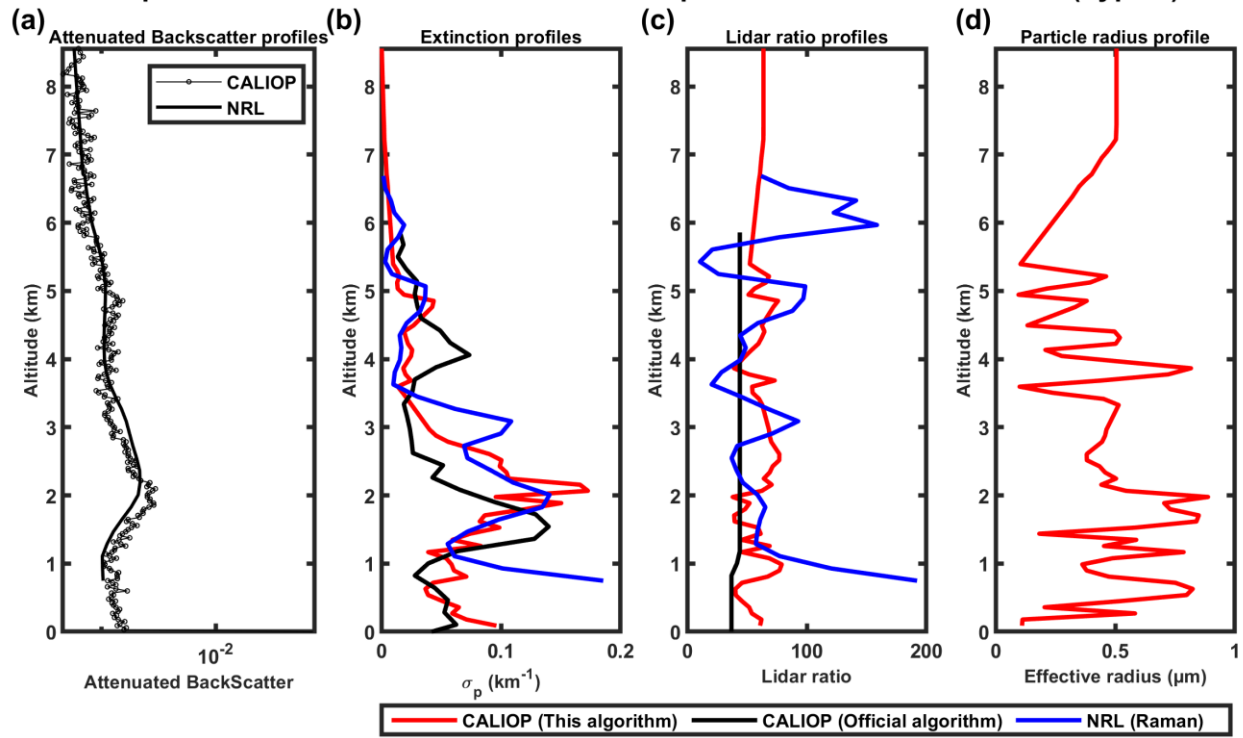
Comparison of CALIOP and EARLINET in Naples at 532nm on 2006-08-20 (Type 1)



462

463 **Figure 9.** 532 nm and 1064 nm attenuated backscatter profiles measured by CALIOP (black solid line with
 464 circle marker) and NRL (remodeling, black solid line) on 20 August 2006 in logarithmic scale in horizontal
 465 direction (a); (b, c, d) show the extinction profiles, lidar ratio profiles and particle radius profiles, respectively,
 466 provided by our inversion algorithm (red), CALIOP operational level 2 product (black) and EARLINET level
 467 2 product (blue).

Comparison of CALIOP and EARLINET in Naples at 532nm on 2007-06-20 (Type 5)



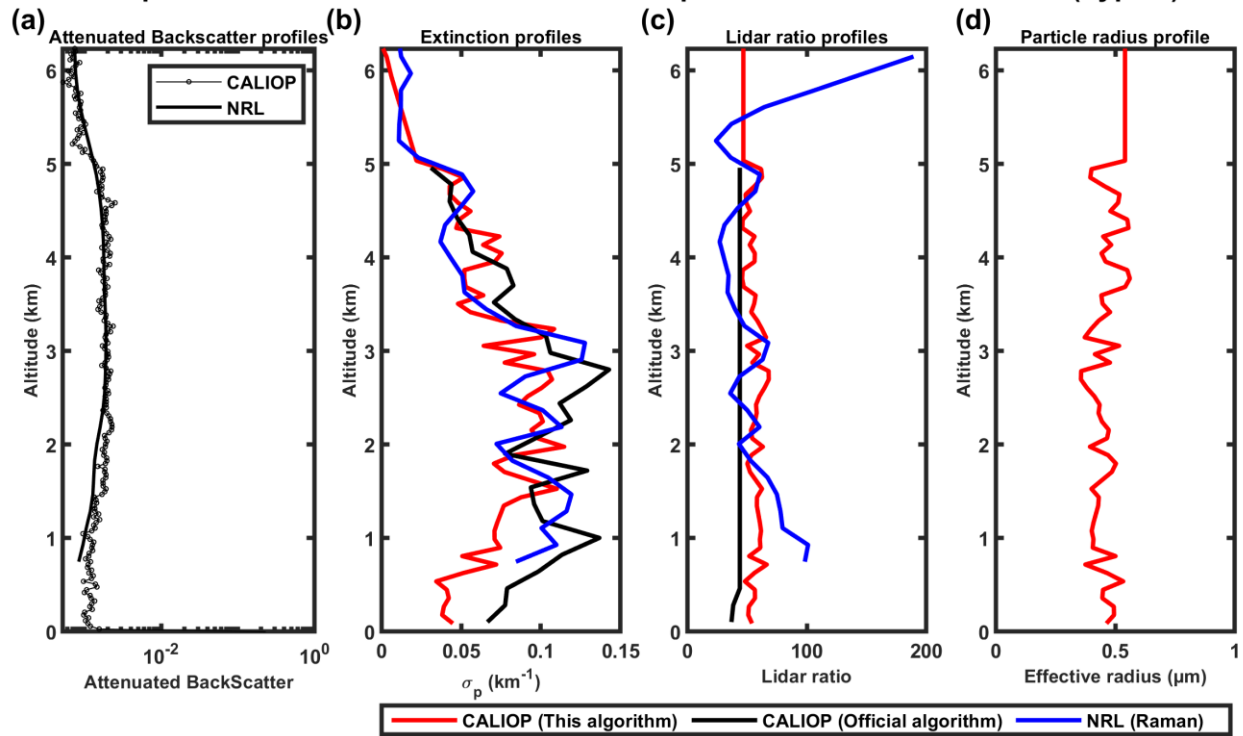
468

469

470

Figure 10. Same as Figure 9 but on 20 June 2007.

Comparison of CALIOP and EARLINET in Naples at 532nm on 2007-07-22 (Type 6)



471

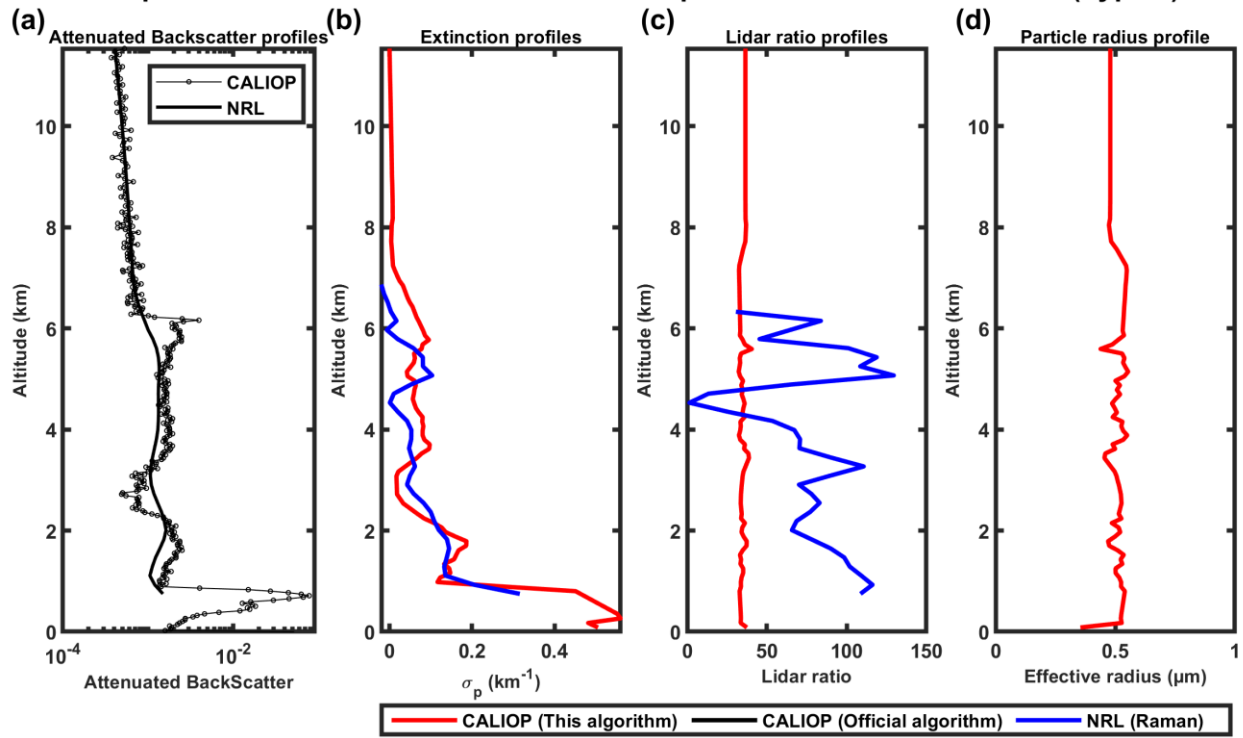
472

473

474

Figure 11. Same as Figure 9 but on 22 July 2007.

Comparison of CALIOP and EARLINET in Naples at 532nm on 2008-07-08 (Type 2)



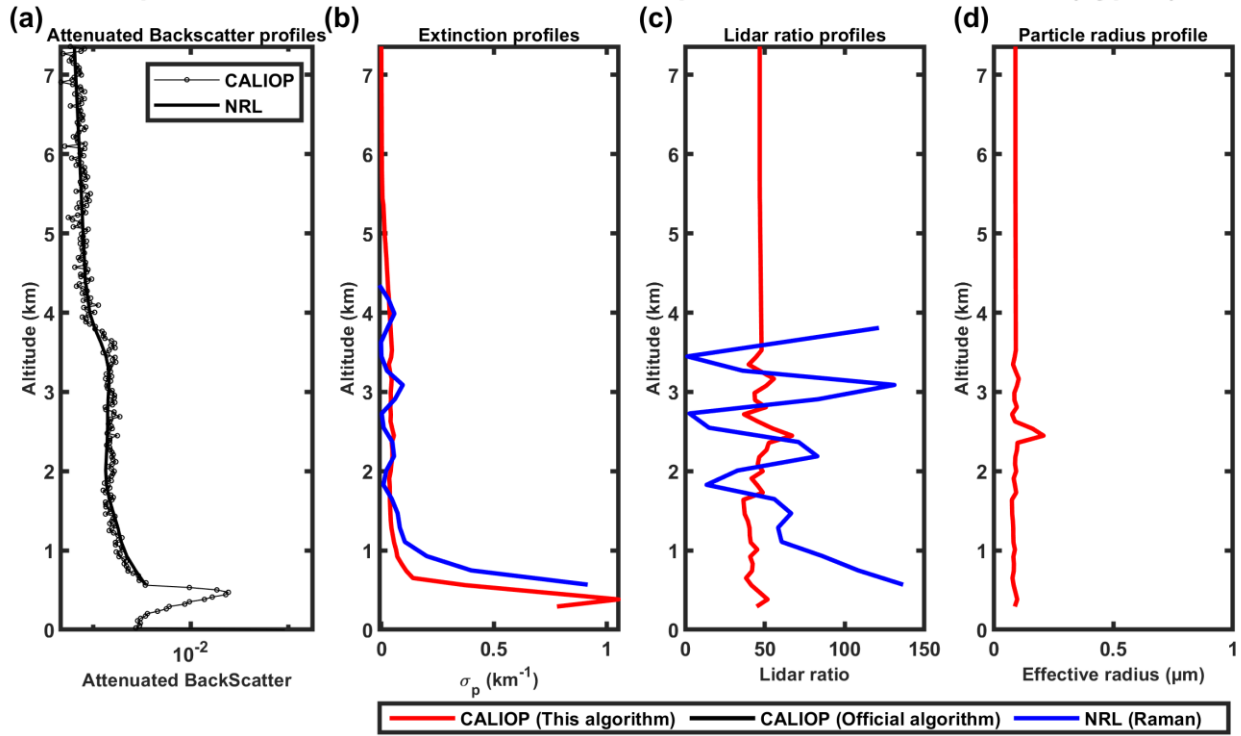
475

476

477

Figure 12. Same as Figure 9 but on 8 July 2008.

Comparison of CALIOP and EARLINET in Naples at 532nm on 2008-08-09 (Type 3)



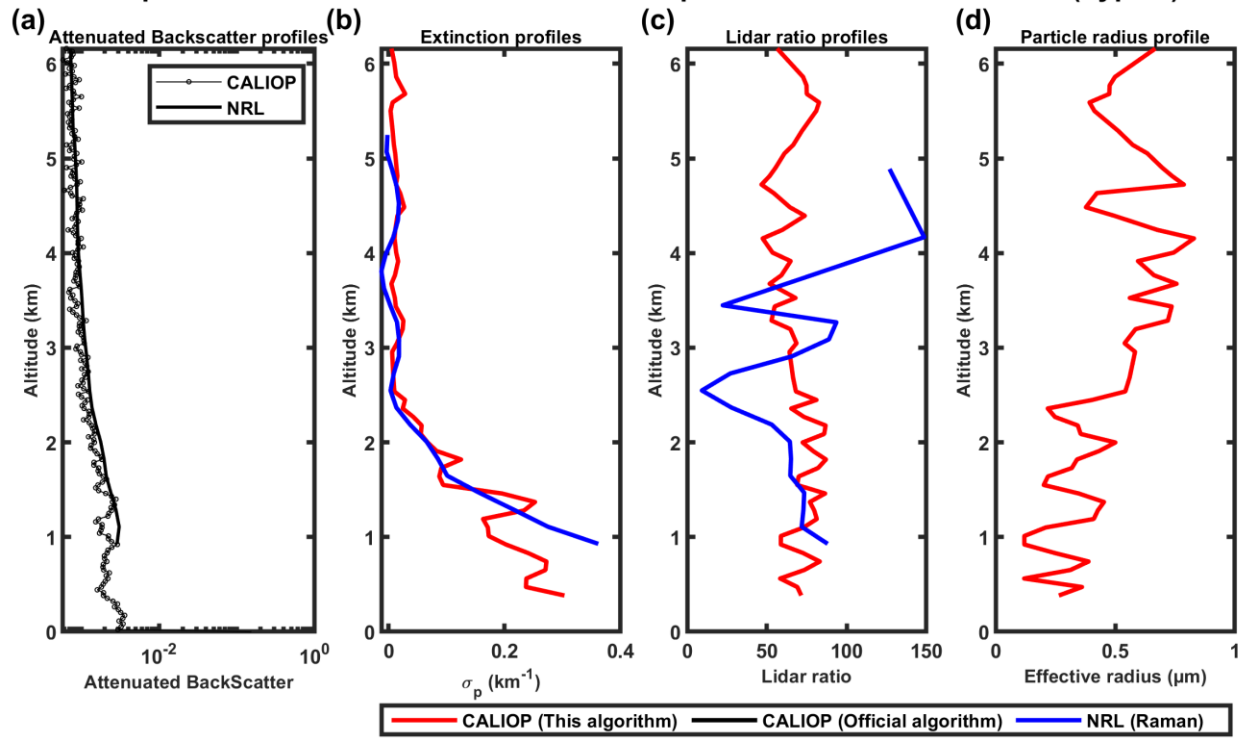
478

479

480

Figure 13. Same as Figure 9 but on 9 August 2008.

Comparison of CALIOP and EARLINET in Naples at 532nm on 2009-09-29 (Type 4)



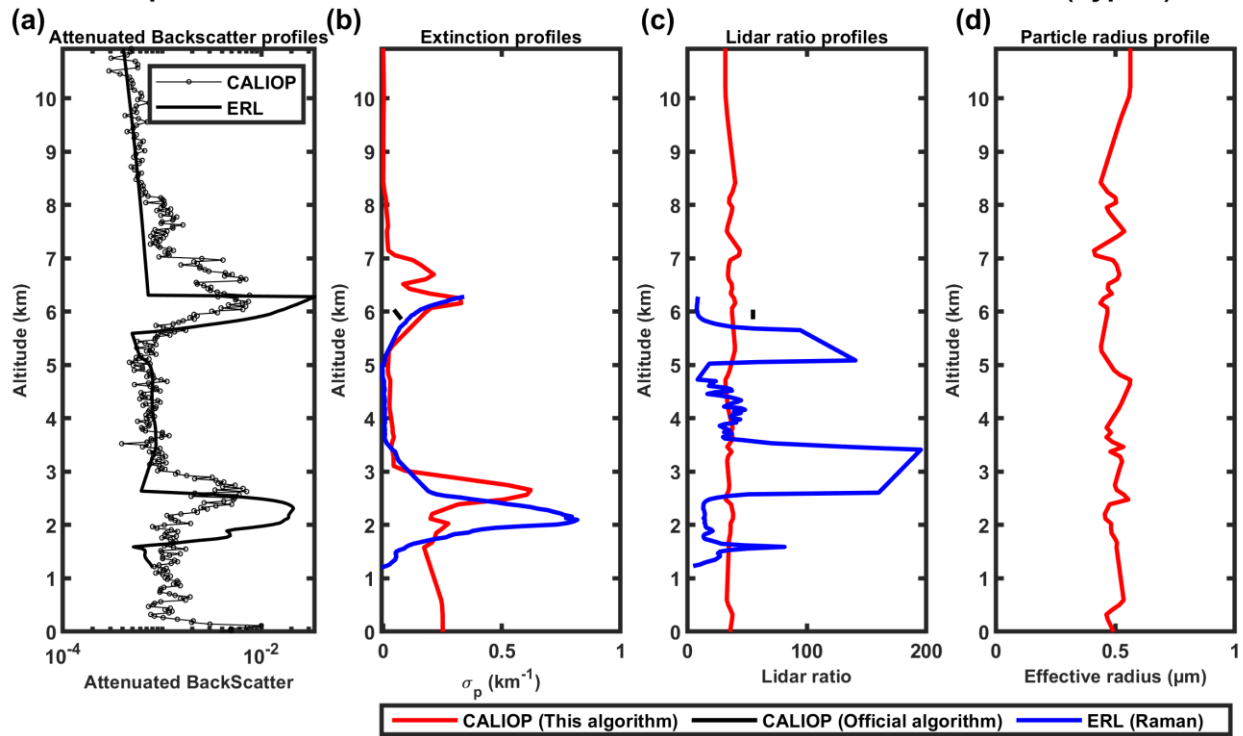
481

482

483

Figure 14. Same as Figure 9 but on 29 September 2009.

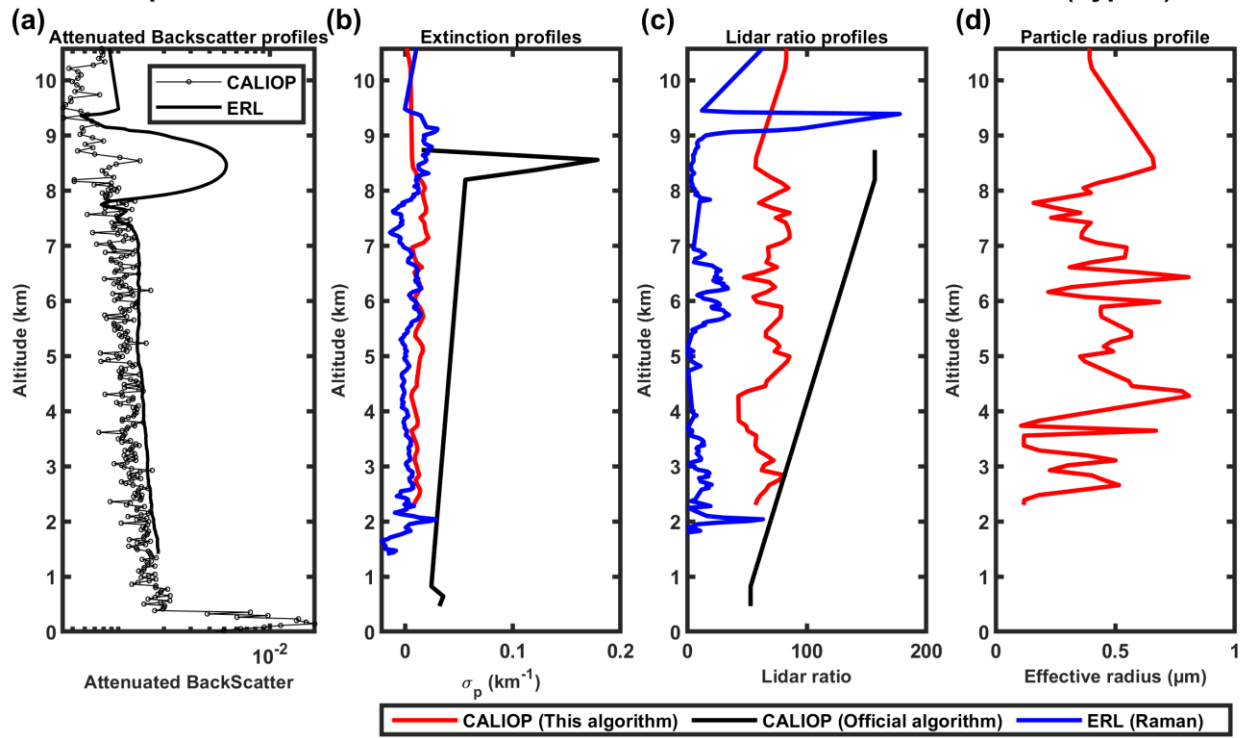
Comparison of CALIOP and EARLINET in Evora at 532nm on 2019-04-05 (Type 2)



484

485 **Figure 15.** 532 nm and 106 nm attenuated backscatter profiles measured by CALIOP (black solid line with
 486 circle marker) and ERL at the Evora station (remodeling, black solid line) on 20 August 2006 in logarithmic
 487 scale in horizontal direction (a); (b, c, d) show the extinction profiles, lidar ratio profiles and particle radius
 488 profiles, respectively, provided by the modified inversion algorithm (red), CALIOP level 2 (black) and
 489 EARLINET level 2 (blue).

Comparison of CALIOP and EARLINET in Evora at 532nm on 2020-01-13 (Type 4)



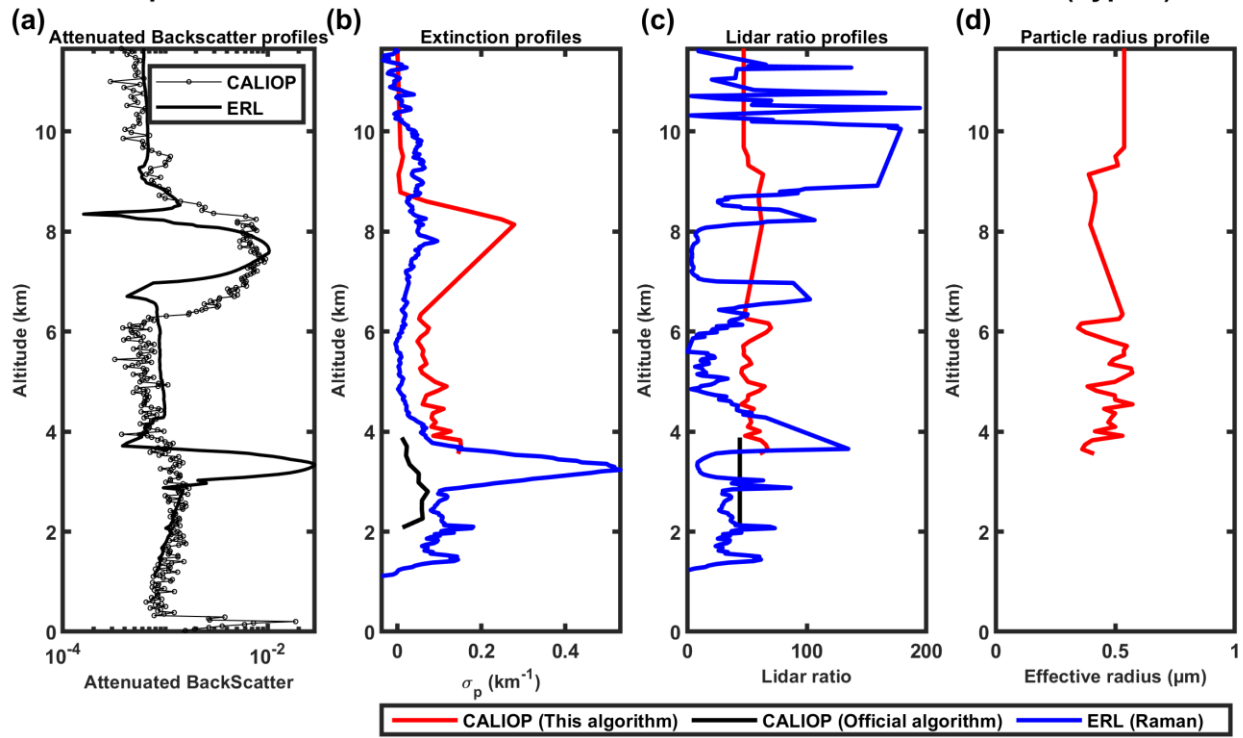
490

491

492

Figure 16. Same as Figure 15 but on 13 January 2020.

Comparison of CALIOP and EARLINET in Evora at 532nm on 2020-03-18 (Type 6)



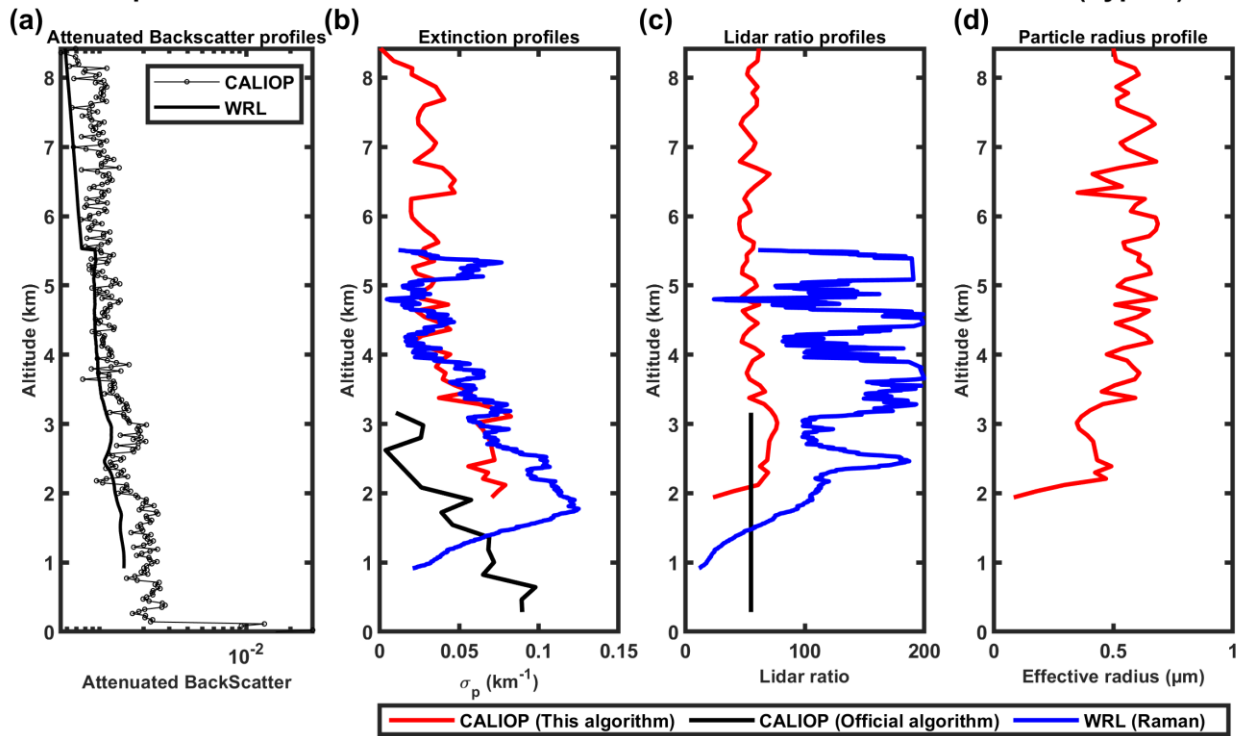
493

494

495

Figure 17. Same as Figure 15 but on 18 March 2020.

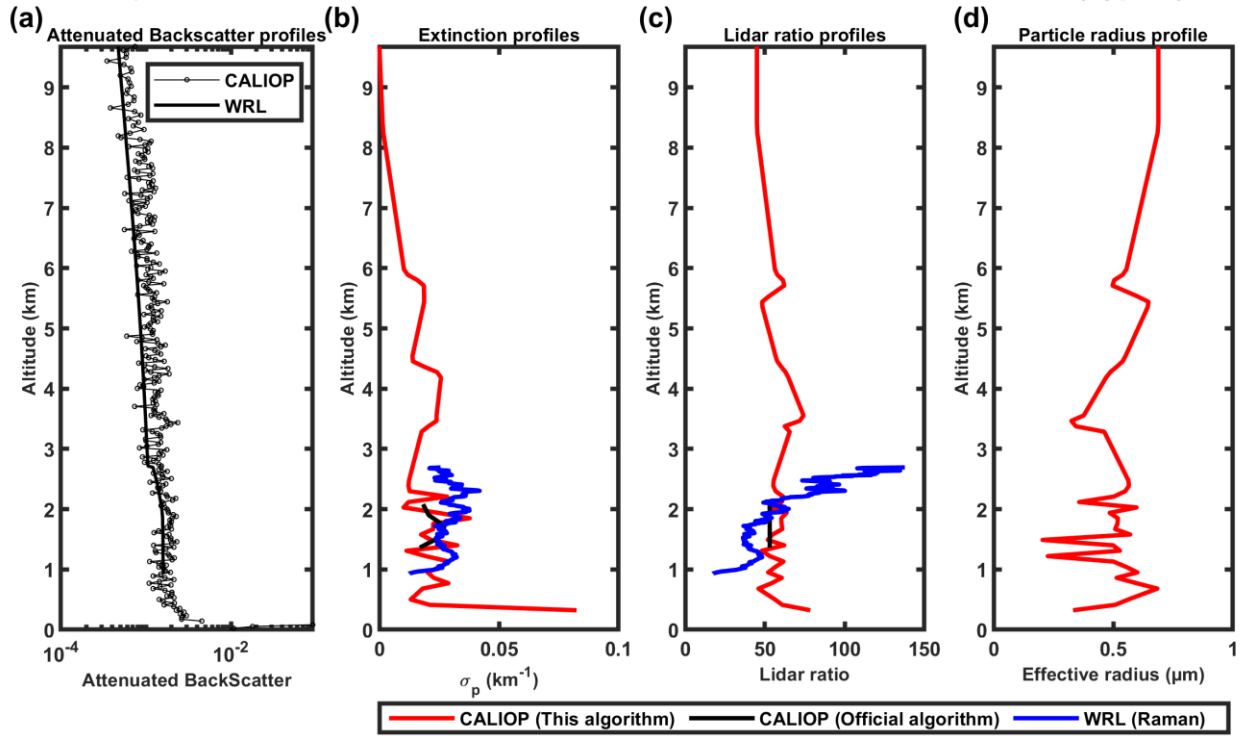
Comparison of CALIOP and EARLINET in Warsaw at 532nm on 2015-08-15 (Type 1)



496

497 **Figure 18.** 532 nm and 106 nm attenuated backscatter profiles measured by CALIOP (black solid line with
 498 circle marker) and WRL at the Warsaw station (remodeling, black solid line) on 20 August 2006 in
 499 logarithmic scale in horizontal direction (a); (b, c, d) show the extinction profiles, lidar ratio profiles and
 500 particle radius profiles, respectively, provided by the modified inversion algorithm (red), CALIOP level 2
 501 (black) and EARLINET level 2 (blue).

Comparison of CALIOP and EARLINET in Warsaw at 532nm on 2020-03-31 (Type 1)



502

503

504

Figure 19. Same as Figure 18 but on 31 March 2020.